Title
Probability density functions for radial anisotropy: implications for the upper 1200 km of the mantle

Journal
Earth and Planetary Science Letters, 217(1-2)

ISSN
0012-821X

Authors
Beghein, Caroline
Trampert, Jeannot

Publication Date
2004

DOI
10.1016/s0012-821x(03)00575-2

Peer reviewed

Probability density functions for radial anisotropy : implications for the upper 1200 km of the mantle

Caroline Beghein *, Jeannot Trampert

Department of Earth Sciences, Utrecht University, Budapestlaan 4, PO Box 80021, 3508 TA Utrecht, The Netherlands

word count : about 280 words in the abstract, 3800 words in the main text, six figures, three tables and 43 references

Abstract

The presence of radial anisotropy in the upper mantle, transition zone and top of the lower mantle is investigated by applying a model space search technique to Rayleigh and Love wave phase velocity models. Probability density functions are obtained independently for S-wave anisotropy, P-wave anisotropy, intermediate parameter η, V_p, V_s and density anomalies. The likelihoods for P-wave and S-wave anisotropy beneath continents cannot be explained by a dry olivine-rich upper mantle at depths larger than 220 km. Indeed, while shear-wave anisotropy tends to disappear below 220 km depth in continental areas, P-wave anisotropy is still present but its sign changes compared to the uppermost mantle. This could be due to an increase with depth of the amount of pyroxene relative to olivine in these regions, although the presence of water, partial melt or a change in the deformation mechanism cannot be ruled out as yet. A similar observation is made for old oceans, but not for young ones where $V_{SH} > V_{SV}$ appears likely down to 670 km depth and $V_{PH} > V_{PV}$ down to 400 km depth. The change of sign in P-wave anisotropy seems to be qualitatively correlated with the presence of the Lehmann discontinuity, generally observed beneath continents and some oceans but not beneath ridges. Parameter η shows a similar age-related depth pattern as shear-wave anisotropy in the uppermost mantle and it undergoes the same change of sign as P-wave anisotropy at 220 km depth. The ratio between $dlnV_s$ and $dlnV_p$ suggests that a chemical component is needed to explain the anomalies in most places at depths greater than 220 km. More tests are needed to infer the robustness of the results for density, but they do not affect the results for anisotropy.

Key words: radial anisotropy, likelihood, upper mantle, transition zone

1 Introduction

Radial anisotropy in the uppermost mantle was first proposed to simultaneously explain fundamental Love and Rayleigh wave phase velocities [1]. PREM [2] was the first reference model to include radial anisotropy in the upper 220 km of the mantle. Since then, numerous surface wave studies showed that this anisotropy varies laterally [3–7] and might extend deeper than 220 km in some areas [3,5], but the exact depth extent is still not clear. It is usually believed that radial anisotropy decreases rapidly with depth. Its presence in the transition zone and in the top of the lower mantle is, however, not excluded, as shown from normal mode data [8] and in regional studies based on shear-wave splitting measurements [9,10]. Higher mode data appear to require radial anisotropy down to about 300 km depth beneath the Indian ocean [5] and the Pacific [11], but not deeper than 220 km depth beneath the Atlantic [7]. Shear-wave anisotropy was also detected in the range 200-400 km depth beneath cratons and 80-200 km under ocean basins in a global study [12].

Current models of radial anisotropy are usually derived from the inversion of surface wave data (fundamental and higher modes). These inversions are inherently non-unique, but the regularisation imposed on the model space to obtain a stable solution chooses one particular model that can explain the data. This can produce discrepancies among different models, especially in the presence of a large model null-space (the part of the model space that is not constrained by the data) and in the case of highly ill-posed problems where the distribution of likely models can be strongly non-Gaussian. Because of this high non-uniqueness, additional constraints are often introduced, sometimes based on physical information but not always. For instance, in inversions for radial anisotropy the number of unknowns is usually reduced by either neglecting model parameters to which the data are the least sensitive and inverting only for two S-wave related parameters and density [11], or by imposing global scalings between perturbations in the different anisotropic parameters [12], based on petrological considerations [13]. These assumptions can restrict the solution to a certain class of models and rule out other solutions a priori.

In this paper, we investigate lateral variations in radial anisotropy in global models using a model space search technique, the Neighbourhood Algorithm (NA) [14,15]. The method was first applied to fundamental mode phase velocity maps to study the upper 220 km of the mantle [16]. The results of this previous study are employed here together with surface wave phase velocity maps constructed from overtone measurements [17] to investigate seismic anisotropy down to approximately 1200 km depth. Because the NA explores the entire

* Corresponding author
Email address: beghein@geo.uu.nl (Caroline Beghein).

ensemble of possible solutions and returns probability density functions for all model parameters, we can deduce robust information on the Earth's average properties within the layers of our parameterization. No relation is assumed between the different anisotropic parameters in order to obtain independent models for S-wave anisotropy and P-wave anisotropy which can be tested against compositional models.

2 Modelling

2.1 Method

The NA [14,15] is a direct search method from which robust information on Earth's properties can be obtained without having to introduce unnecessary a priori information in the model space. Details on the method are given in the two original papers [14,15] and in normal mode and surface wave applications [18,19]. The NA consists of two stages. During the first stage, the model space is surveyed and regions that best fit the data are identified. Provided the right tuning parameters, the NA finds all models compatible with the data. One can explore different parts of the model space simultaneously and there is always a possibility to move towards more promising regions. The number of models generated automatically increases in the vicinity of the good fitting areas. After the sampling of the model space, a "misfit map" is obtained, and models of high misfit are associated with a small likelihood, while models with lower misfit are associated with a higher likelihood. An importance sampling of this ensemble of models is then performed in the second stage of the NA to generate a resampled ensemble whose distribution follows the distribution of misfit previously obtained. This resampled ensemble is integrated numerically to compute the posterior probability density (PPD) functions associated with each model parameter and the covariance matrix that gives the trade-offs among the different variables. Because the second stage is highly time-consuming, the NA limits the size of the model space which can be studied in a reasonable amount of time. It can, however, be easily applied to phase velocity maps as they can be expanded into spherical harmonics. The inverse problem is then solved separately for each spherical harmonic coefficient of Earth's structure.

2.2 Data

The data set employed is composed of the isotropic part of azimuthally anisotropic phase velocity maps constructed from higher mode measurements [17] for

Rayleigh and Love waves of overtone number $n = 1$ and $n = 2$. The technique to obtain these phase velocity maps is described in [20,21]. The isotropic part of the phase velocity models were developed on a spherical harmonic (SH) basis up to degree 40 and coefficients up to degree 8 (not affected by regularisation in the phase velocity maps) are employed here to constrain Earth's structure. It can be shown that the degree s and order t of the phase velocity perturbation ${}_k\left(\frac{\delta c}{c}\right)^t_s$ is linearly related to perturbations in Earth's structure at degree s and order t :

$$ {}_k\left(\frac{\delta c}{c}\right)^t_s = \int_0^a \delta \mathbf{m}^t_s(r) {}_k\mathbf{K}(r) r^2 \, dr \tag{1} $$

where k discriminates between different surface wave frequencies, a is the radius of the Earth and ${}_k\mathbf{K}(r)$ is the partial derivative, or depth sensitivity kernels, for model parameter $\delta \mathbf{m}^t_s(r)$.

Errors in phase velocity models are best evaluated by comparing different models. Due to the lack of other overtone phase velocity maps, data errors are assumed to be identical to errors previously determined for fundamental Love and Rayleigh wave phase velocity maps at the corresponding periods [18]. A previous study [22] showed that this assumption is reasonable for degree zero. We assume here that it is also valid for other SH coefficients. For periods of 40, 60, 80, 100 and 150 seconds fundamental mode surface wave phase velocity models from different studies [17,23–25,21,26–28] were averaged and a standard deviation was computed for each SH coefficient. As in [18], data uncertainties at degree s and azimuthal order t are assumed to be independent of t, and an average over t is calculated. At intermediate periods we made a simple interpolation of the uncertainties obtained at 40, 60, 80, 100 and 150 seconds. At periods higher than 150 seconds we imposed the same error as the one estimated at 150 seconds (see [18] for explanations).

The data are corrected with crustal model CRUST5.1 [29]. Since the size of the model space which can be surveyed with the NA is limited, and since we do not want to neglect parameters or impose any scaling between the different anisotropic parameters, we reduce the number of unknowns by further correcting the data with models of radial anisotropy previously obtained for the uppermost mantle [16]. These models were derived by applying the NA to fundamental mode Love and Rayleigh wave phase velocity models to constrain radial anisotropy in the top 220 km of the mantle. The likelihoods obtained for each model parameter, at each SH coefficient up to degree 8, are resampled to compute distributions of predictions of overtone measurements for the uppermost mantle (UMM). From each distribution (approximately Gaussian) we calculate a mean contribution $\mathbf{d}^{\mathbf{UMM}}$ and a standard deviation $\sigma^{\mathbf{UMM}}$ which are employed to correct the data :

$$\mathbf{d^{res}} = \mathbf{d^0} - \mathbf{d^{CRUST5.1}} - \mathbf{d^{UMM}} \quad (2)$$

$$\sigma^{\mathbf{res}} = \sigma^{\mathbf{0}} + \sigma^{\mathbf{UMM}} \quad (3)$$

$\mathbf{d^0}$ and $\sigma^{\mathbf{0}}$ represent the original data and data uncertainty. $\mathbf{d^{CRUST5.1}}$ represents the contribution of the crust. Original errors are incremented to account for the uncertainties on the models of UMM anisotropy. We thus invert residual data $\mathbf{d^{res}}$ and associated errors $\sigma^{\mathbf{res}}$ with the NA to find models of radial anisotropy between 220 and 1200 km depth. By proceeding in such a way, we do not fix the UMM with one particular model that would influence the results at larger depths due to trade-offs between model parameters. Instead, we include in $\sigma^{\mathbf{res}}$ and $\mathbf{d^{res}}$ all possible "good" models for the upper 220 km, and the PPD functions obtained for the deeper mantle are representative of all acceptable models below 220 km depth.

2.3 Parameterization

Radial anisotropy can be described by five independent elastic coefficients A, C, N, L and F [30]. C and A are related to the wavespeed of P-waves travelling vertically (V_{PV}) and horizontally (V_{PH}), respectively. L and N give the wavespeed of vertically (V_{SV}) and horizontally (V_{SH}) polarized shear waves and F describes waves travelling with an intermediate incidence angle. We parameterized the models as perturbations of the Love parameters and perturbations of density with respect to PREM [2]. The model parameters are expanded on a spherical harmonic basis, and the relation between the data and the structure of the Earth is :

$$\begin{aligned} {}_k\left(\frac{\delta c}{c}\right)_s^t = \int_{r_{cmb}}^{r_{220}} [\ {}_kK_A(r)\delta A_s^t(r) + {}_kK_C(r)\delta C_s^t(r) + {}_kK_N(r)\delta N_s^t(r) \\ + {}_kK_L(r)\delta L_s^t(r) + {}_kK_F(r)\delta F_s^t(r) + {}_kK_\rho(r)\delta\rho_s^t(r)]r^2\,dr \end{aligned} \quad (4)$$

where the integration is done between the core-mantle boundary (r_{cmb} is the radius of core-mantle boundary) and 220 km depth.

Parameters $\xi = 1-N/L$, $\phi = 1-C/A$ and $\eta = 1-F/(A-2L)$ are reconstructed a posteriori. Parameter ξ describes the anisotropy of shear waves, ϕ P-wave anisotropy and η intermediate anisotropy. Note that the definition of these parameters vary from author to author. In the convention used here, if there is no anisotropy ξ, ϕ and η are zero. Negative values of ξ correspond to $V_{SH} > V_{SV}$ and positive values of ϕ correspond to $V_{PH} > V_{PV}$. As an example, $\xi = -0.05$ means that horizontally polarized shear-waves travel 5 % faster than vertically polarized shear-waves.

A layered parameterization is adopted with three layers delimited by the following depths : 220-400 km, 400-670 km and 670-1230 km. We therefore have 18 model parameters (six parameters in three layers) for each SH component. The choice of this layered division was not based on the depth resolution of the data, but was mainly motivated by computational resources. Our parameterization is still sufficient to analyze the robustness of the anisotropic signal. We tested that a coarse layering returns the representative averages of finer layers. This is because we get all models compatible with the data and thus no bias occurs because of the chosen parameterisation. Still, a detailed geodynamical interpretation will clearly need a more refined analysis.

2.4 Retrieving anisotropy, velocity and density anomalies

The same procedure as in [16] is applied. The NA provides PPD functions associated to each SH component of the model parameters : δA_s^t, δC_s^t, δN_s^t, δL_s^t, δF_s^t and $\delta \rho_s^t$. Random values of these δm_s^t are generated, using their exact PPD functions, and the SH coefficients are recombined to get $\delta m(r, \theta, \phi)$. The parameters describing radial anisotropy are then recovered by computing ξ, ϕ and η at each point (r, θ, ϕ) in the Earth. Equivalent isotropic P-wave and S-wave velocity anomalies, together with density anomalies, are also calculated at (r, θ, ϕ). Histograms are then computed by repeating the procedure described above several thousand times, and for every model generated the function of interest (anisotropy, velocity or density anomalies) is averaged over a particular area (e.g. continents, oceans,...). The distributions represent thus the range of data-compatible values of this function, averaged over a certain area, and do not account for structure variations within the area considered.

3 Results

Figures 1 to 6 represent the likelihoods obtained for parameter ξ, ϕ and η in various tectonic regions, selected from model 3SMAC [31]. On top of the three layers employed here, we plot the results obtained in a previous study for the uppermost mantle [16] and used to reduce the overtone data. Table 1 displays the probability that a given parameter is negative, computed by integration of the normalized likelihoods. Different tests showed that anomalies in S-wave related parameters (L and N) have very little trade-offs with other model parameters and that they are well-resolved (narrow marginals) by the data, indicating the robustness of the results for S-wave anisotropy. More caution is necessary for the other model parameters since not all SH coefficients are well constrained (wide marginals) for dA, dC, dF and $d\rho$.

Figure 1 shows the likelihood of S-wave anisotropy in the different layers, beneath continents. The data do not require S-wave anisotropy below 220 km depth in most continental regions, except maybe beneath cratons where the probability to have $\xi < 0$, therefore $V_{SH} > V_{SV}$, is 0.65 between 220 and 400 km depth (see Table 1). This possibly indicates that shear-wave anisotropy, with fast horizontally polarized shear waves, extends a little deeper than the Lehmann discontinuity in PREM [2] beneath cratons, but not beneath younger continental areas. There is further a small probability that ξ becomes positive in the transition zone beneath cratons. The signal is much clearer beneath oceans, as shown in Figure 2 where oceanic regions are separated according to the age of the overlying ocean floor. We see that there is a strong probability of $V_{SH} > V_{SV}$ between depths of 220 and 400 km and in the transition zone. The anisotropy between 220 and 400 km depth is smaller than on top, but its presence is still likely (see also Table 1). In the transition zone, we clearly observe $\xi < 0$ beneath young oceans, with amplitudes comparable to the ones obtained between 100 and 220 km depth. An age-dependent signal is also detected in the transition zone since the probability of $\xi < 0$ decreases for older oceanic regions.

Figures 3 and 4 give the likelihoods associated with P-wave anisotropy beneath continents and oceans, respectively. There is a high probability of negative ϕ beneath continents in the depth range 220-400 km, and possibly in the transition zone. This corresponds to fast vertically travelling P-waves ($V_{PV} > V_{PH}$) and indicates a change of sign in ϕ with respect to the uppermost mantle. An age-related signal is observed for oceanic regions, between 220 and 400 km depth. ϕ seems most likely positive beneath young oceans and tends to become most likely negative in older regions, similar to continents. $\phi < 0$ also appears to extend in the transition zone beneath old and intermediate oceans, but not as clearly as at shallower depths.

In Figure 5, η clearly changes sign between the uppermost mantle and larger depths, in continental areas. It stays negative down to 1230 km depth beneath platforms and tectonically active regions, and maybe beneath cratons but with a smaller probability. Similar to ϕ, parameter η is most likely positive beneath young oceans and becomes most likely negative in old regions (Figure 6). A strong signal with $\eta < 0$ is also observed at depths between 670 and 1230 km. However, as mentioned above, parameters dA, dC and dF are less well determined (wider marginals) than dL and dN. The likelihoods obtained for ϕ and η by recombining individual likelihoods for different elastic parameters could therefore be dominated by only a few well-resolved SH coefficients.

Analysis of the correlation matrices obtained for the individual SH coefficients (not displayed here) shows very little little trade-off between the three layers, indicative of a depth resolution approximately equal to the width of the layers. Histograms for the likelihood of correlation between $dlnV_p$, $dlnV_s$ and

$dln\rho$ were also computed and showed a good global correlation between $dlnV_p$ and $dlnV_s$, but poor correlation between density and velocity anomalies, in the three layers. It was demonstrated with synthetic tests [19] that density anomalies could be recovered using normal mode data, overtone and fundamental surface wave data together. Further tests are needed to see whether fundamental mode and overtone phase velocity data alone can determine density. We thus refrain here from a further interpretation of density results. Importantly, extensive tests showed that density did not influence any elastic parameter in this study.

4 Implications for the upper 1200 km of the mantle

The novelty of our approach is the presentation of the models in terms of PPD functions, which allows to test possible explanations more quantitatively.

Considering isotropic velocities first, if the anomalies in $dlnV_s$ and $dlnV_p$ would be thermal in origin, one would expect the highest probability for $dlnV_s/dlnV_p$ to be between 1 and 2 [32]. This is clearly not the case below 220 km depth (Tables 2 and 3), and in most places in the uppermost mantle. We therefore suggest that a chemical component is responsible for a good part of the observed signal.

An age-related anisotropic signal is likely beneath oceanic areas for S-wave anisotropy, going as deep as the transition zone. Indeed, we observe shear wave anisotropy with fast horizontally polarized shear waves down to 670 km beneath young oceans, but probably not much deeper than 400 km depth beneath older oceans. The anisotropy in the transition zone is thus stronger and more likely beneath young oceans than beneath older ones. The depth pattern of ξ beneath oceans younger than 50 Ma is characterized by a minimum between 220 and 400 km depth, similar to the one found by other authors for azimuthal anisotropy [20]. The fact that the anisotropy varies with the age of the ocean floor in the transition zone, and that the anisotropic signal observed in the UMM seems to extend deeper beneath young oceans but not beneath old ones, could be an indication that ridges have some deep connection. This connection is most likely chemical in origin as inferred from Table 3. A better resolution of the anomalies at these depths is, however, required to draw more robust conclusions. No strong S-wave anisotropy is required by the data beneath continents at depths larger than 220 km, except perhaps beneath cratons where there is some evidence for shear-wave anisotropy with $V_{SH} > V_{SV}$. This could reflect the age-related depth extent of continents.

Although our most likely model of shear-wave anisotropy resembles models of the UMM previously obtained by inversions [12,33], there are significant

differences at larger depths. For instance, the model obtained by Gung & Romanowicz [12] presents shear-wave anisotropy with $V_{SV} > V_{SH}$ beneath the East Pacific Rise at 300 km depth, while our most likely model favours $V_{SH} > V_{SV}$ beneath ridges at these depths. Our results beneath continents (with slightly deeper anisotropy beneath cratons than beneath younger regions) seem to agree more with theirs. Although their model does not agree with our most likely model, it is compatible with our PPD functions since the probability of having $V_{SV} > V_{SH}$ beneath young oceans in the depth range 220-400 km is non zero (see Table 1). The differences most likely originate from the methods employed, i.e. regularisation in traditional inversions and scaling relationships imposed between the parameters. Another difference is the inclusion of body wave data in the study of Gung & Romanowicz [12] and not present here.

One of the great advantages of the method employed here is that we obtained PPD functions for P-wave anisotropy, for η and for S-wave anisotropy independently, i.e. without assuming a priori any relation between the different anisotropic parameters. By comparing the relative behaviour of ξ, ϕ and η we can gain important information on the Earth's interior. We find that there is no systematic relation between perturbation in parameters η, ϕ and ξ, as sometimes assumed in some inversions [12], which means that the data do not support any particular scaling relationship between $d\eta$, $d\phi$ and $d\xi$. In the upper 220 km we simultaneously find $V_{SH} > V_{SV}$ and $V_{PH} > V_{PV}$ in all regions, which is typical of an olivine-rich uppermost mantle, and which is usually considered as evidence for horizontal flow in the absence of water inclusions. However, the relationship between P-wave anisotropy and S-wave anisotropy appears to change below 220 km depth beneath continents and possibly benath old oceans. The clear change of sign in P-wave anisotropy observed beneath continents at about 220 km depth while shear wave anisotropy is most likely zero (or very small) is not compatible with the traditional upper mantle dominated by dry olivine aligned by lattice preferred orientation (LPO). Possible interpretations include the presence of water or partial melt which was shown to modify the alignement of olivine by shear stress [34,35]. A change in the deformation mechanism yielding different anisotropic signals could also be responsible [36]. To data these studies are not sufficiently advanced to make a clear case.

We suggest that a chemical stratification of the upper mantle beneath continents and beneath old oceans is another possibility. As mentioned by other authors [37], the two main models of mantle petrology, i.e. the pyrolite model (olivine-rich) and the piclogite model (more clinopyroxene than olivine), can be tested against seismic models. In particular P-wave anisotropy should be more sensitive to compositional changes than S-wave anisotropy. Experiments of LPO [37] show that both orthopyroxene (Opx) and clinopyroxene (Cpx) interfere destructively with P-wave anisotropy of olivine because their fast di-

rection for V_P is orthogonal to the [100] axis of olivine. Shear-wave anisotropy is destroyed by the presence of Cpx, but not by Opx which interferes constructively. For this reason we suggest the presence of a transition between an olivine-rich UMM and a lower upper mantle enriched in pyroxene beneath continents (and possibly old oceans). Since our PPD functions show that S-wave anisotropy in these regions is either very small or zero between 220 and 400 km depth, it is tempting to favour Cpx over Opx. However, the lack of data for the anisotropic properties of Cpx makes a robust interpretation in terms of Cpx or Opx still difficult. Interestingly, an enrichment in Cpx with depth would agree with geological studies of the slave craton [38]. A similar division between a pyrolite uppermost mantle and a piclogite model below was previously proposed [39], but these inferences were based on the isotropic velocities and the anisotropy of the global model PREM [2]. Nevertheless, because pyroxenes have less intrinsic anisotropy than olivine and since they do not develop strong LPO [37], a lot of pyroxene would be needed to explain our models. Final quantitative estimates are, however, still difficult to date.

As opposed to old oceans, young oceans appear be compatible with a pyrolite model down to 400 km depth since the usual relation between S and P-wave anisotropy for olivine appears to be preserved. The $V_{SH} > V_{SV}$ and $V_{PH} > V_{PV}$ signal observed down to 400 km depth beneath oceanic ridges could then be explained by a vertical flow in the presence of partial melt which tends to align olivine a-axes at 90° to the shear direction [35]. Note that this significantly different from inferences from isotropic tomography which sees ridges as shallow features [40]. The transition zone would then correspond to the usually assumed olivine to wadsleyite to ringwoodite phase transformations. A combination between wadsleyite and ringwoodite could explain the strong S-wave anisotropy and the weak P-wave anisotropy [37]. Horizontal layering can be excluded to explain the detected anisotropy in the transition zone because it would not result in the observed azimuthal anisotropy [20] and one would expect to find P-wave anisotropy as well.

Finally, it is interesting to note that the places where we find a change in the sign of ϕ (continents and old oceans) are globally correlated to the places where the Lehmann discontinuity is detected [41,42], and the places where seismic anisotropy seems to vary more smoothly with depth (beneath ridges) correspond to regions where the discontinuity is not detected. We also find a qualitatively good correlation between the age-related depth extent of shear-wave anisotropy and the depth at which the Lehmann discontinuity is observed [41]. This could indicate a connection between the Lehmann discontinuity and chemical variations in the upper mantle and it contradicts the hypothesis that the discontinuity marks a transition from deformation by dislocation creep to diffusion creep [43].

5 Aknowledgments

This research would not have been possible without M. Sambridge's code, which he kindly makes available. We thank H.J. van Heijst for his overtone measurements and S.-I. Karato and A. Tommasi for interesting discussions. Comments from B. Kennett and an anonymous reviewer helped to improve the manuscript.

References

[1] D. L. Anderson, Elastic wave propagation in layered anisotropic media, J. Geophys. Res. 66 (1961) 2,953–2,963.

[2] A. M. Dziewonski, D. L. Anderson, Preliminary reference Earth model, Phys. Earth Planet. Inter. 25 (1981) 25,297–25,356.

[3] J.-P. Montagner, T. Tanimoto, Global upper mantle tomography of seismic velocities and anisotropies, J. Geophys. Res. 96 (B12) (1991) 20,337–20,351.

[4] M. Cara, A. Nercessian, G. Nolet, New inferences from higher mode data in western Europe and northern Eurasia, Geophys. J. R. astr. Soc. 61 (1980) 459–478.

[5] J.-J. Lévêque, E. Debayle, V. Maupin, Anisotropy in the Indian Ocean upper mantle from Rayleigh- and Love-waveform inversion, Geophys. J. Int. 133 (1998) 529–540.

[6] E. Debayle, B. L. N. Kennett, Anisotropy in the Australasian upper mantle from Love and Rayleigh waveform inversion, Earth Planet. Sci. Lett. 184 (2000) 339–351.

[7] G. Silveira, E. Stutzmann, Anisotropic tomographic of the Atlantic Ocean, Phys. Earth Planet. Inter. 132 (2002) 237–248.

[8] J.-P. Montagner, B. L. N. Kennett, How to reconcile body-wave and normal-mode reference Earth models, Geophys. J. Int. 125 (1996) 229–248.

[9] J. Wookey, J.-M. Kendall, G. Barruol, Mid-mantle deformation inferred from seismic anisotropy, Nature 415 (2002) 777–780.

[10] W.-P. Chen, M. R. Brudzinski, Seismic anisotropy in the mantle transition zone beneath Fiji-Tonga, Geophys. Res. Lett. 30 (13) (2003) 1682,doi:10.1029/2002GL016330.

[11] J.-P. Montagner, Seismic anisotropy of the Pacific Ocean inferred from long-period surface waves dispersion, Phys. Earth Planet. Inter. 38 (1985) 28–50.

[12] Y. Gung, M. Panning, B. Romanowicz, Global anisotropic and the thickness of continents, Nature 422.

[13] J.-P. Montagner, D. L. Anderson, Petrological constraints on seismic anisotropy, Phys. Earth Planet. Inter. 54 (1989) 82–105.

[14] M. Sambridge, Geophysical inversion with a neighbourhood algorithm-I. Searching a parameter space, Geophys. J. Int. 138 (1999) 479–494.

[15] M. Sambridge, Geophysical inversion with a neighbourhood algorithm-II. Appraising the ensemble, Geophys. J. Int. 138 (1999) 727–746.

[16] C. Beghein, J. Trampert, Probability density functions for radial anisotropy from fundamental mode surface wave data and the neighbourhood algorithm, Geophys. J. Int. Submitted.

[17] H. J. van Heijst, J. H. Woodhouse, Global high-resolution phase velocity distributions of overtone and fundamental-mode surface waves determined by mode branch-stripping, Geophys. J. Int. 137 (1999) 601–620.

[18] C. Beghein, J. Resovsky, J. Trampert, P and S tomography using normal mode and surface wave data with a neighbourhood algorithm, Geophys. J. Int. 149 (2002) 646–658.

[19] J. S. Resovsky, J. Trampert, Reliable mantle density error bars : An application of the Neighbourhood Algorithm to normal mode and surface wave data, Geophys. J. Int. 150 (2002) 665–672.

[20] J. Trampert, H. J. van Heijst, Global azimuthal anisotropy in the transition zone, Science 296 (2002) 1,297–1,299.

[21] J. Trampert, J. H. Woodhouse, Global anisotropic phase velocity maps for fundamental mode surface waves between 40 and 150 seconds, Geophys. J. Int. 154 (2003) 154–165.

[22] C. Beghein, J. Trampert, A radial anisotropic reference model of the mantle using normal mode and surface wave data with a neighbourhood algorithm, Geophys. J. Int. Submitted.

[23] J. Trampert, J. H. Woodhouse, Global phase velocity maps of Love and Rayleigh waves between 40 and 150 seconds, Geophys. J. Int. 122 (1995) 675–690.

[24] J. Trampert, J. H. Woodhouse, High resolution global phase velocity distributions, Geophys. Res. Lett. 23 (1996) 21–24.

[25] J. Trampert, J. H. Woodhouse, Assessment of global phase velocity models, Geophys. J. Int. 144 (2001) 165–174.

[26] G. Ekström, J. Tromp, E. W. F. Larson, Measurements and global models of surface wave propagation, J. Geophys. Res. 102 (1997) 8,137–8,157.

[27] G. Laske, G. Masters, Constraints on global phase velocity maps from long-period polarization data, J. Geophys. Res. 101 (1996) 16,059–16,075.

[28] Y. K. Wong, Upper mantle heterogeneity from phase and amplitude data of mantle waves, Ph.D. thesis, Harvard Univ. (1989).

[29] W. Mooney, G. Laske, G. Masters, Crust 5.1 : a global crustal model at 5 deg ×5 deg, J. Geophys. Res. 103 (B1) (1998) 727–747.

[30] A. E. H. Love, A Treatise on the Theory of Elasticity, Cambridge Univ. Press, 1927.

[31] H.-C. Nataf, Y. Ricard, 3SMAC : an a priori tomographic model of the upper mantle based on geophysical modeling, Phys. Earth Planet. Inter. 95 (1996) 101–122.

[32] S.-I. Karato, B. Karki, Origin of lateral variation of seismic wave velocities and density in the deep mantle, J. Geophys. Res. 106 (B10) (2001) 21,771–21,783.

[33] G. Ekström, A. M. Dziewonski, The unique anisotropy of the Pacific upper mantle, Nature 394 (1998) 168–172.

[34] H. Jung, S.-I. Karato, Water-induced fabric transitions in olivine, Science 293 (2001) 1460–1463.

[35] B. K. Holtzman, D. L. Kohlstedt, M. E. Zimmerman, F. Heidelbach, T. Hiraga, J. Hustoft, Melt segregation and strain partioning : implications for seismic anisotropy and mantle flow, Science 301 (2003) 1,227–1,230.

[36] M. K. Savage, Seismic anisotropy and mantle deformation : what have we learned from shear wave splitting?, Rev. Geophys. 37 (1999) 65–106.

[37] D. Mainprice, G. Barruol, W. B. Ismaïl, The seismic anisotropy of the Earth's mantle : from single crystal to polycrystal, in: S. Karato (Ed.), Earth's Deep Interior: Mineral Physics and Tomography From the Atomic to the Global Scale, Seismology and Mineral Physics, Geophys. Monogr. Ser., Vol. 117, AGU, Washington, D.C., 2000, pp. 237–264.

[38] S. Y. O'Reilly, W. L. Griffin, Y. H. P. Djomani, P. Morgan, Are lithosphere forever?, GSA Today. (2001) 4–10April.

[39] L. H. Estey, B. J. Douglas, Upper mantle anisotropy : a preliminary model, J. Geophys. Res. 91 (1986) 11,393–11,406.

[40] J.-P. Montagner, J. Ritsema, Interactions between ridges and plumes, Science 294 (2001) 1,472–1,473.

[41] J. Revenaugh, T. H. Jordan, mantle layering from ScS reverberations- 3. The upper mantle, J. Geophys. Res. 96 (B12) (1991) 19,781–19,810.

[42] A. Deuss, J. H. Woodhouse, A systematic search for mantle discontinuities using SS-precursors, Geophys. Res. Lett. 29 (2002) 10.1029/2002GL014768.

[43] S.-I. Karato, On the Lehmann discontinuity, Geophys. Res. Lett. 19 (22) (1992) 2,255–2,258.

Fig.1 : Likelihood of S-wave anisotropy beneath continents. The vertical line represents the value of PREM averaged over the layers.

Fig.2 : Likelihood of S-wave anisotropy beneath oceans. The vertical line represents the value of PREM averaged over the layers.

Fig.3 : Likelihood of P-wave anisotropy beneath continents. The vertical line represents the value of PREM averaged over the layers.

Fig.4 : Likelihood of P-wave anisotropy beneath oceans. The vertical line represents the value of PREM averaged over the layers.

Fig.5 : Likelihood of η-anisotropy beneath continents. The vertical line represents the value of PREM averaged over the layers.

Fig.6 : Likelihood of η-anisotropy beneath oceans. The vertical line represents the value of PREM averaged over the layers.

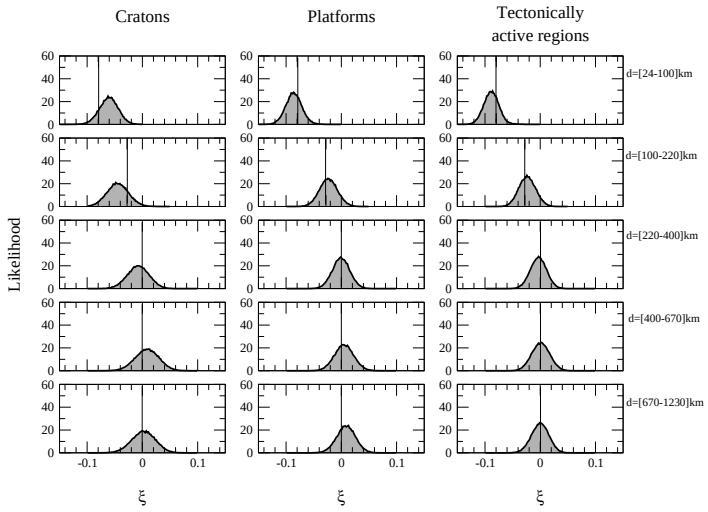
Cratons
Platforms
Tectonically active regions
Likelihood
d=[24-100]km
d=[100-220]km
d=[220-400]km
d=[400-670]km
d=[670-1230]km
ξ

Fig. 1.

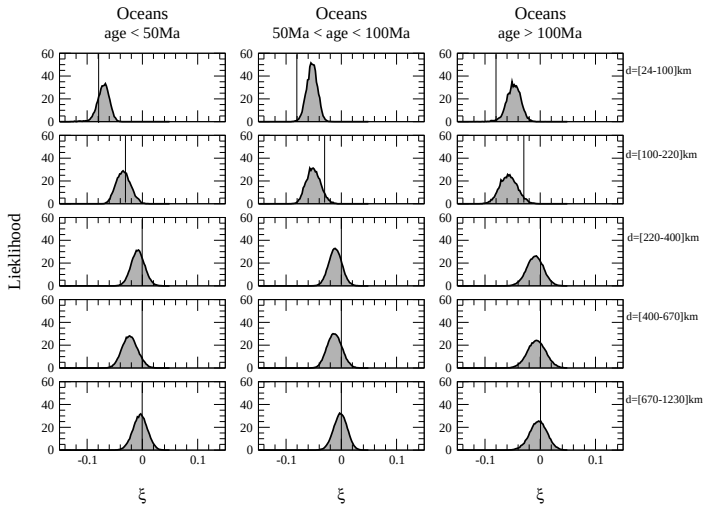
Oceans age < 50Ma
Oceans 50Ma < age < 100Ma
Oceans age > 100Ma
Likelihood
d=[24-100]km
d=[100-220]km
d=[220-400]km
d=[400-670]km
d=[670-1230]km
ξ

Fig. 2.

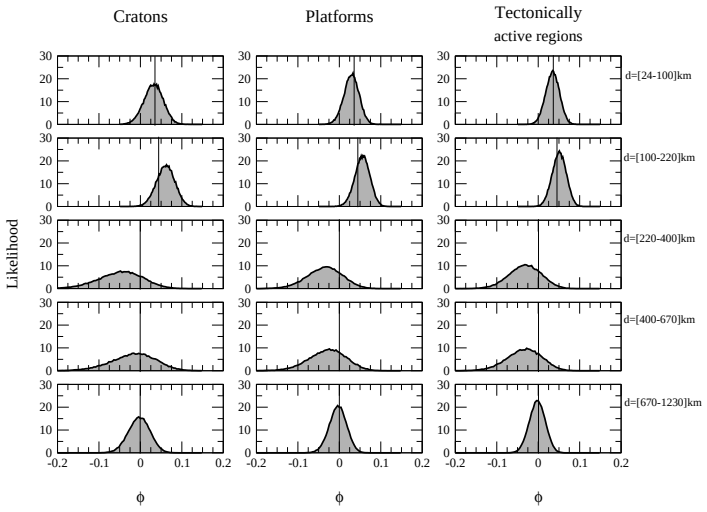
Cratons
Platforms
Tectonically
active regions
d=[24-100]km
d=[100-220]km
d=[220-400]km
d=[400-670]km
d=[670-1230]km
Likelihood
ϕ

Fig. 3.

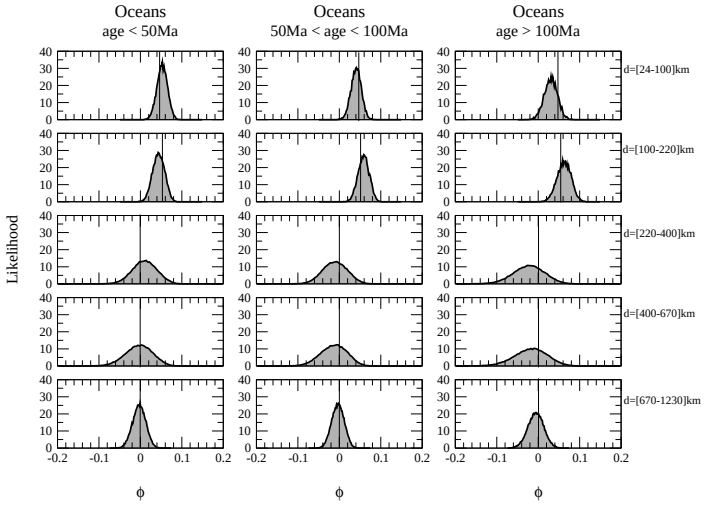
Oceans
age < 50Ma
Oceans
50Ma < age < 100Ma
Oceans
age > 100Ma
d=[24-100]km
d=[100-220]km
d=[220-400]km
d=[400-670]km
d=[670-1230]km
Likelihood
ϕ

Fig. 4.

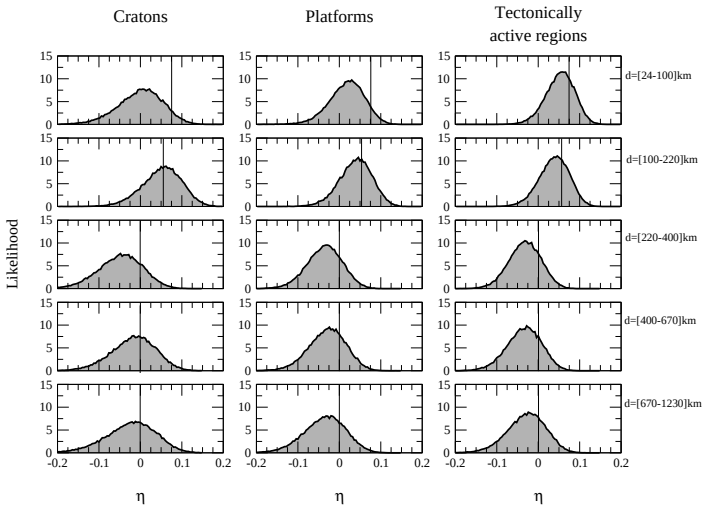
Cratons
Platforms
Tectonically active regions
Likelihood
d=[24-100]km
d=[100-220]km
d=[220-400]km
d=[400-670]km
d=[670-1230]km
η

Fig. 5.

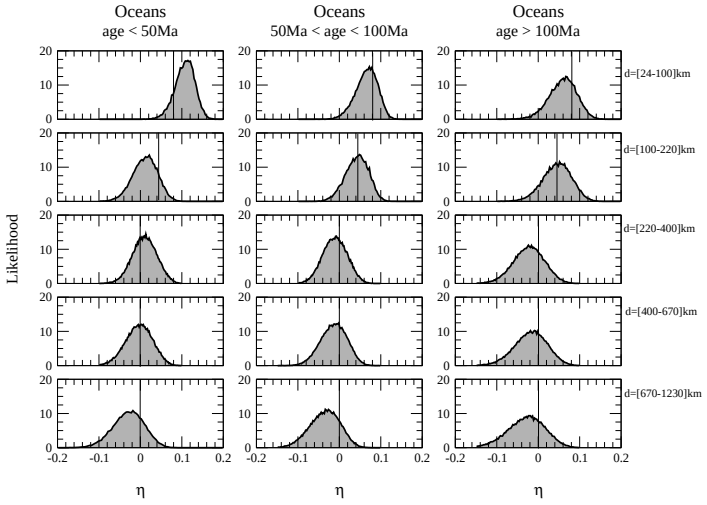
Oceans age < 50Ma
Oceans 50Ma < age < 100Ma
Oceans age > 100Ma
Likelihood
d=[24-100]km
d=[100-220]km
d=[220-400]km
d=[400-670]km
d=[670-1230]km
η

Fig. 6.

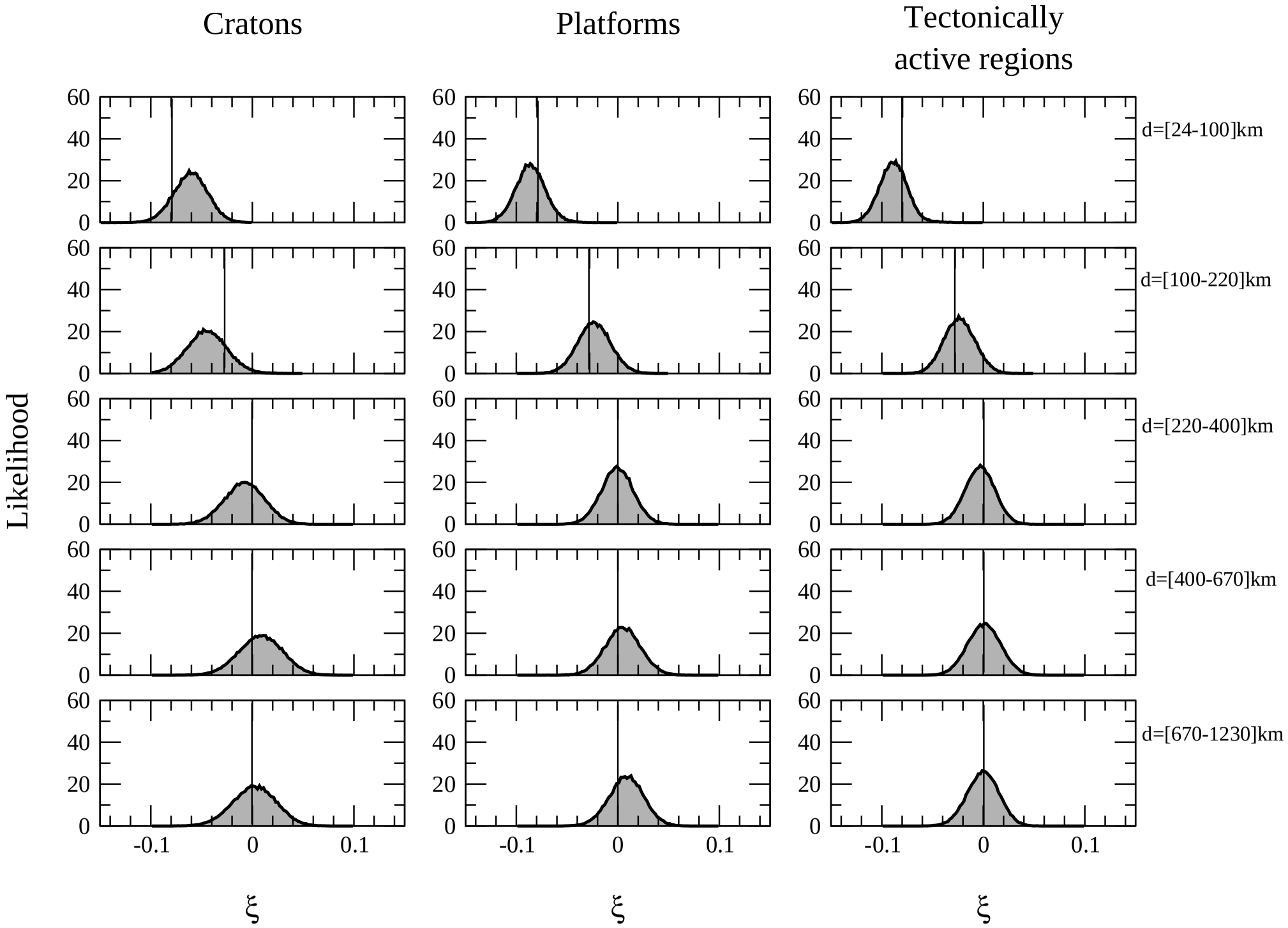
Cratons
Platforms
Tectonically active regions
Likelihood
d=[24-100]km
d=[100-220]km
d=[220-400]km
d=[400-670]km
d=[670-1230]km
60
40
20
0
-0.1
0
0.1
ξ

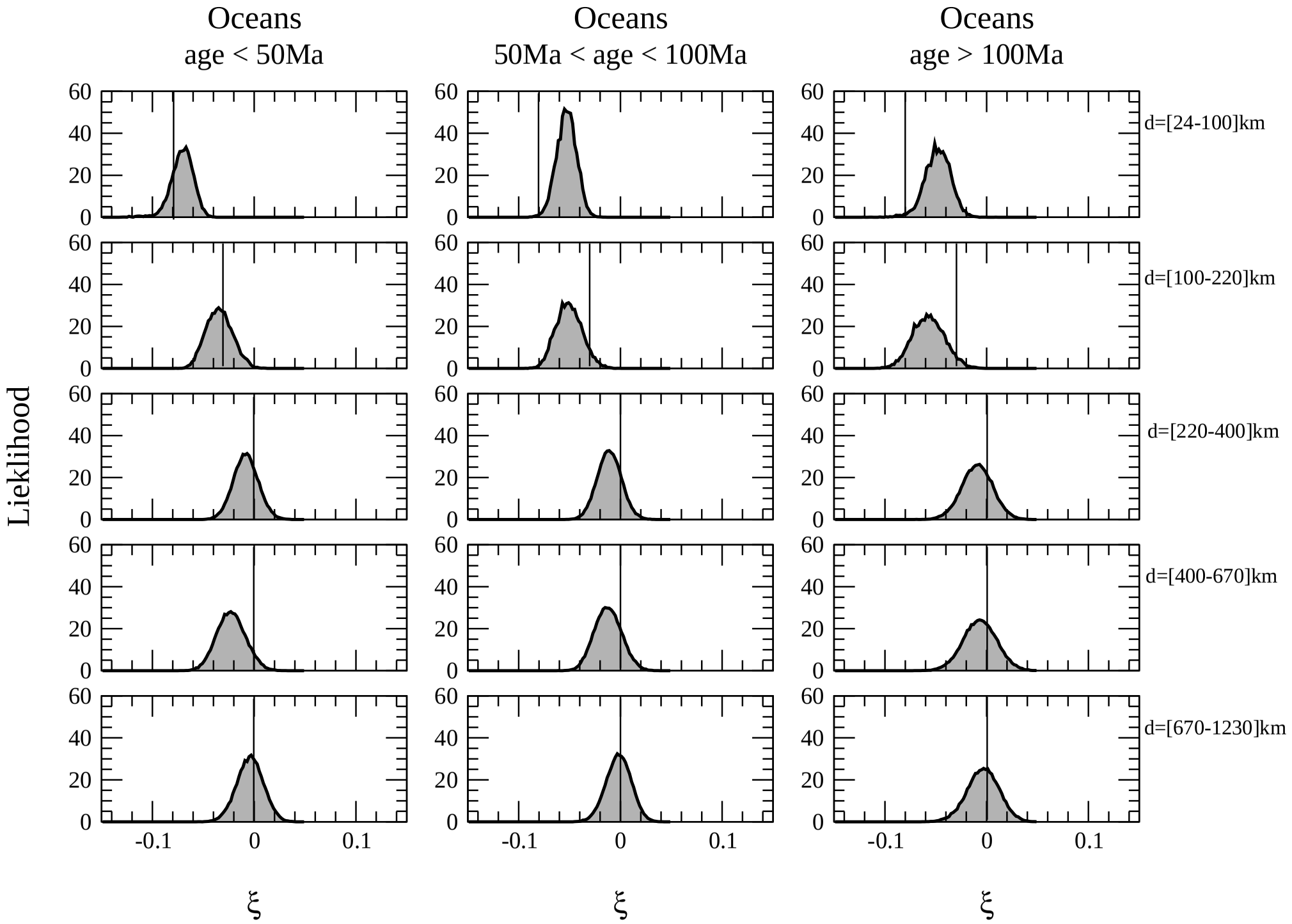
Oceans
age < 50Ma
Oceans
50Ma < age < 100Ma
Oceans
age > 100Ma
Lieklihood
d=[24-100]km
d=[100-220]km
d=[220-400]km
d=[400-670]km
d=[670-1230]km
60
40
20
0
-0.1
0
0.1
ξ

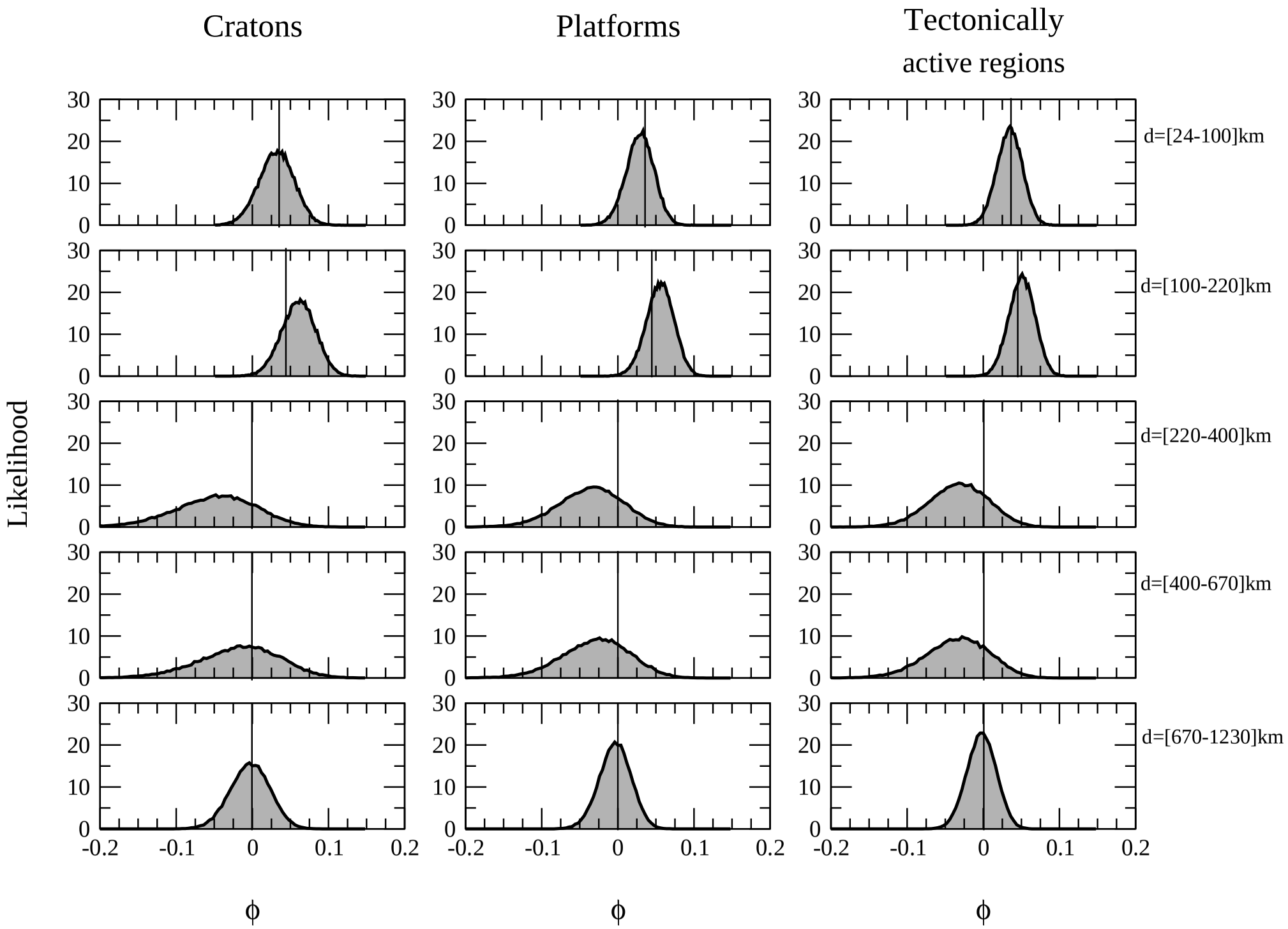
Cratons
Platforms
Tectonically active regions
Likelihood
d=[24-100]km
d=[100-220]km
d=[220-400]km
d=[400-670]km
d=[670-1230]km
0
10
20
30
-0.2
-0.1
0
0.1
0.2
ϕ

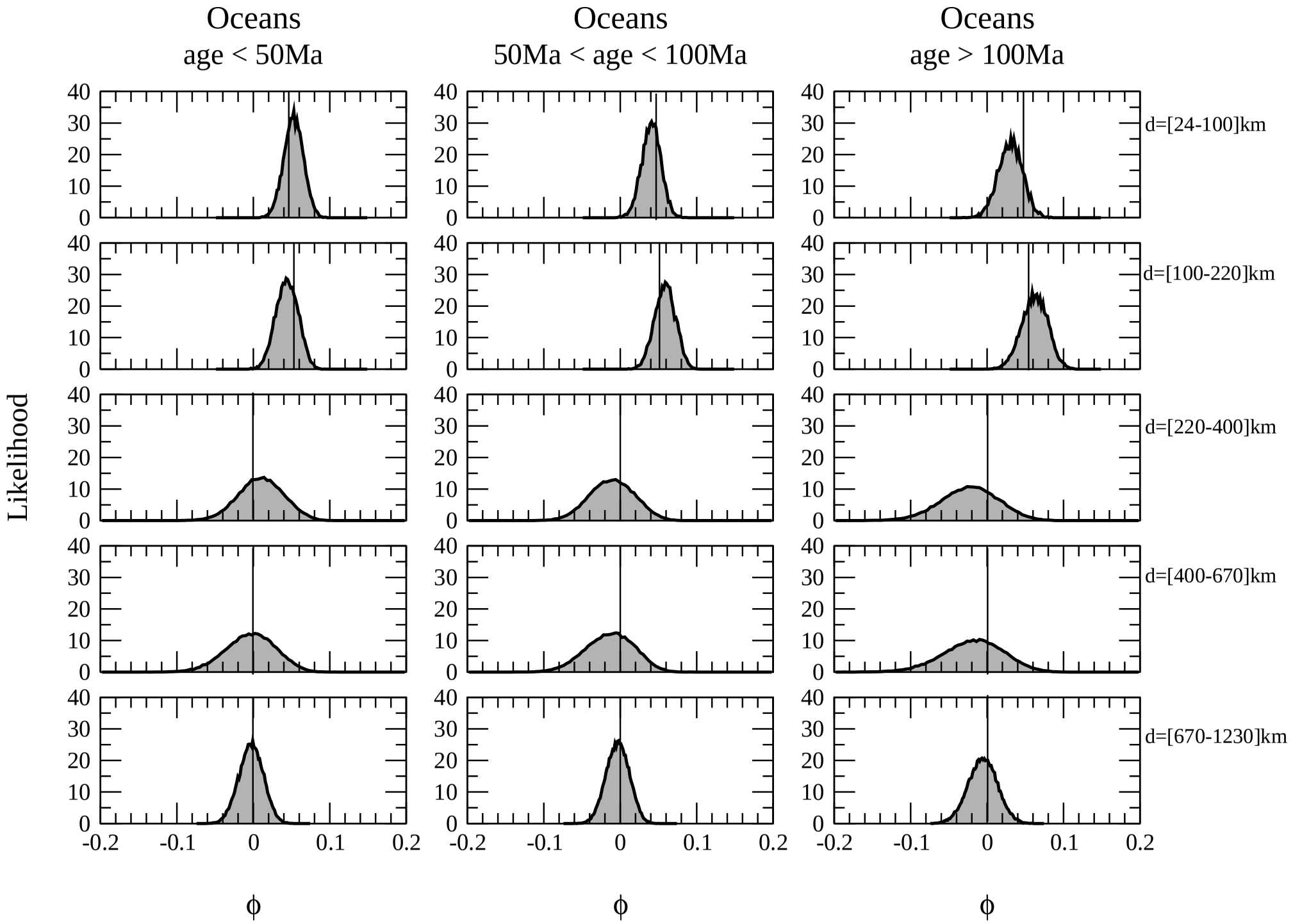
Oceans
age < 50Ma
Oceans
50Ma < age < 100Ma
Oceans
age > 100Ma
Likelihood
d=[24-100]km
d=[100-220]km
d=[220-400]km
d=[400-670]km
d=[670-1230]km
0
10
20
30
40
-0.2
-0.1
0
0.1
0.2
ϕ

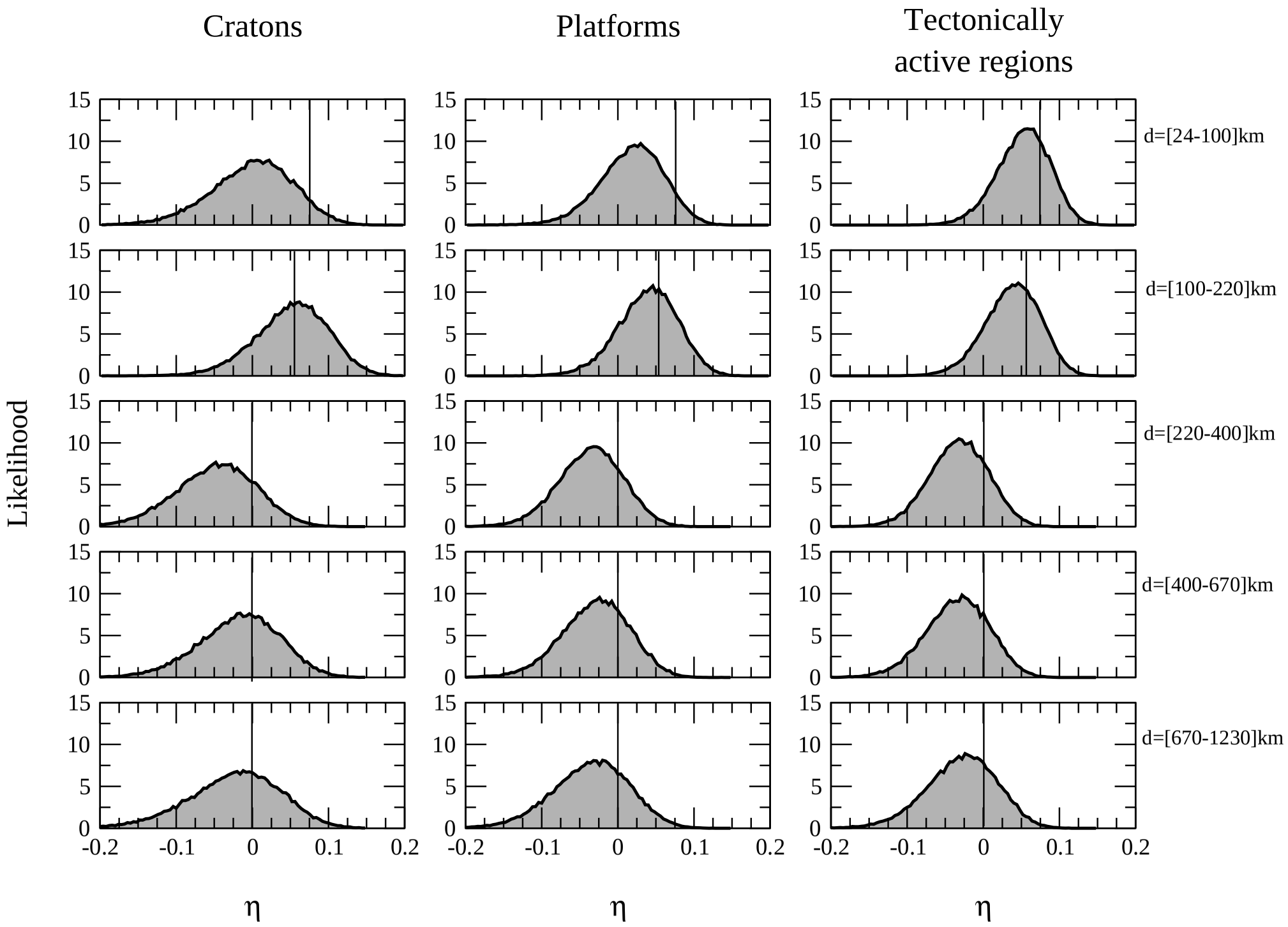
Cratons
Platforms
Tectonically active regions
Likelihood
d=[24-100]km
d=[100-220]km
d=[220-400]km
d=[400-670]km
d=[670-1230]km
0
5
10
15
-0.2
-0.1
0
0.1
0.2
η

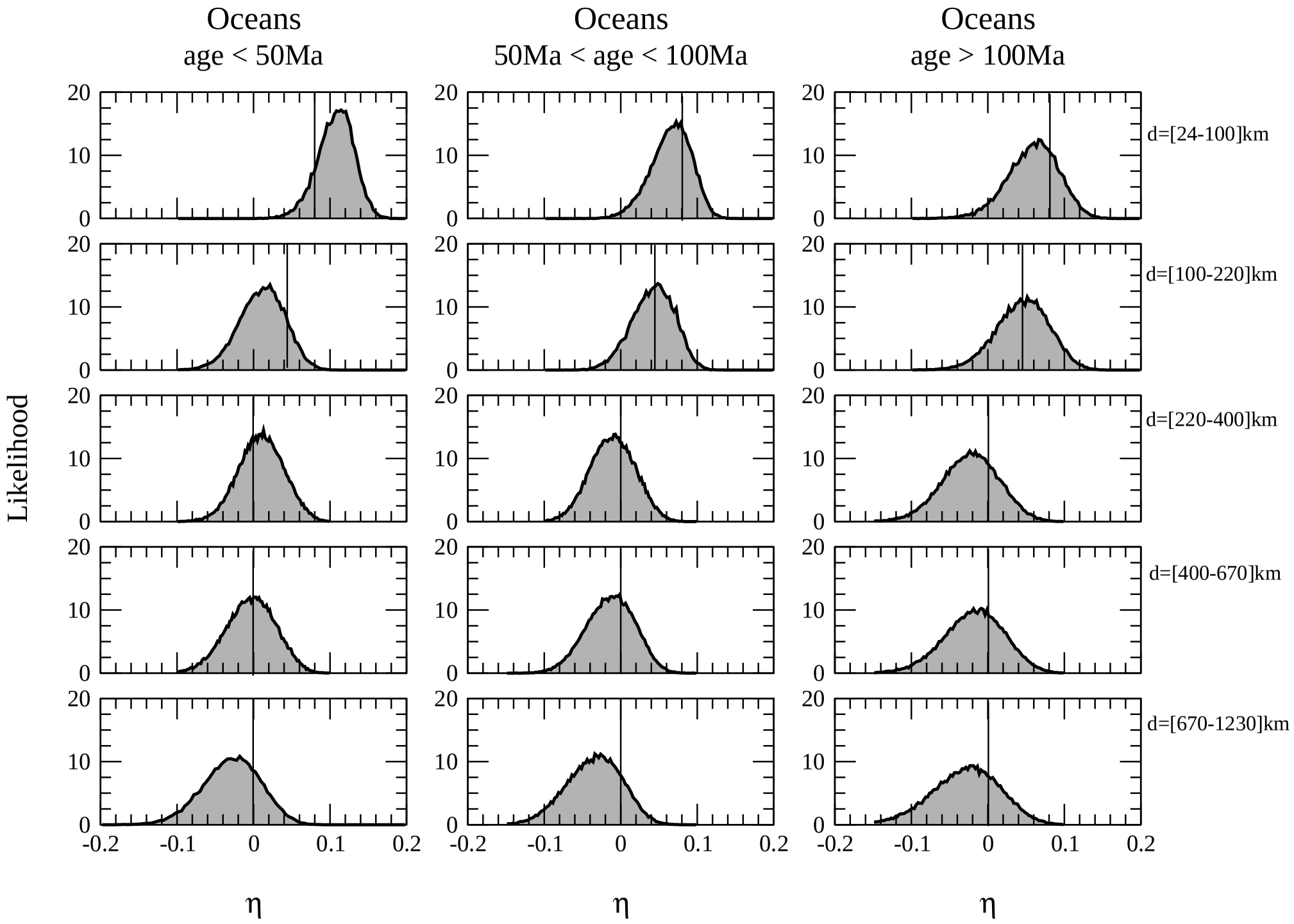
Oceans
age < 50Ma
Oceans
50Ma < age < 100Ma
Oceans
age > 100Ma
Likelihood
d=[24-100]km
d=[100-220]km
d=[220-400]km
d=[400-670]km
d=[670-1230]km
0
10
20
-0.2
-0.1
0
0.1
0.2
η

Parameter p	Depth (km)	Area	$P(p<0)$	Area	$P(p<0)$
$\xi =$	$220<d<400$	All cratons	0.65	All oceans	0.71
$1-N/L$	$400<d<670$		0.35	younger than 50 Ma	0.93
	$670<d<1230$		0.46		0.62
	$220<d<400$	All platforms	0.54	All oceans	0.80
	$400<d<670$		0.39	50 Ma<age<100 Ma	0.83
	$670<d<1230$		0.31		0.54
	$220<d<400$	All tectonically	0.59	All oceans	0.73
	$400<d<670$	active regions	0.48	older than 100 Ma	0.66
	$670<d<1230$		0.52		0.58
$\phi =$	$220<d<400$	All cratons	0.79	All oceans	0.37
$1-C/A$	$400<d<670$		0.60	younger than 50 Ma	0.53
	$670<d<1230$		0.55		0.59
	$220<d<400$	All platforms	0.79	All oceans	0.62
	$400<d<670$		0.60	50 Ma<age<100 Ma	0.65
	$670<d<1230$		0.60		0.57
	$220<d<400$	All tectonically	0.80	All oceans	0.72
	$400<d<670$	active regions	0.77	older than 100 Ma	0.66
	$670<d<1230$		0.61		0.61
$\eta =$	$220<d<400$	All cratons	0.79	All oceans	0.38
$1-F/(A-2L)$	$400<d<670$		0.60	younger than 50 Ma	0.53
	$670<d<1230$		0.63		0.78
	$220<d<400$	All platforms	0.79	All oceans	0.65
	$400<d<670$		0.75	50 Ma<age<100 Ma	0.66
	$670<d<1230$		0.77		0.84
	$220<d<400$	All tectonically	0.80	All oceans	0.75
	$400<d<670$	active regions	0.77	older than 100 Ma	0.66
	$670<d<1230$		0.72		0.73

Table 1
Probability of having parameter $p<0$. The probabilities above 220 km depth are taken from [16]

Depth (km)	Area	$P\left(\frac{dlnV_s}{dlnV_p} < 0\right)$	$P\left(0 < \frac{dlnV_s}{dlnV_p} < 1\right)$	$P\left(1 < \frac{dlnV_s}{dlnV_p} < 2\right)$	$P\left(\frac{dlnV_s}{dlnV_p} > 2\right)$
$24 < d < 100$	All cratons	0.0	0.0	0.49	0.51
$100 < d < 220$		0.0	0.0	0.74	0.26
$220 < d < 400$		0.34	0.23	0.21	0.22
$400 < d < 670$		0.16	0.37	0.29	0.18
$670 < d < 1230$		0.23	0.38	0.20	0.19
$24 < d < 100$	All platforms	0.0	0.0	0.32	0.68
$100 < d < 220$		0.0	0.0	0.69	0.31
$220 < d < 400$		0.29	0.08	0.22	0.41
$400 < d < 670$		0.19	0.32	0.29	0.20
$670 < d < 1230$		0.24	0.44	0.23	0.09
$24 < d < 100$	All tectonically	0.25	0.58	0.15	0.02
$100 < d < 220$	active regions	0.14	0.46	0.34	0.06
$220 < d < 400$		0.36	0.26	0.20	0.18
$400 < d < 670$		0.23	0.32	0.23	0.22
$670 < d < 1230$		0.18	0.40	0.19	0.23

Table 2
Probabilities for $dlnV_s/dlnV_p$ beneath continents. Velocity anomalies were calculated for degrees 1 to 8 with respect to PREM. The probabilities above 220 km depth are taken from [16].

Depth (km)	Area	$P\left(\frac{dlnV_s}{dlnV_p} < 0\right)$	$P\left(0 < \frac{dlnV_s}{dlnV_p} < 1\right)$	$P\left(1 < \frac{dlnV_s}{dlnV_p} < 2\right)$	$P\left(\frac{dlnV_s}{dlnV_p} > 2\right)$
$24 < d < 100$	All oceans	0.06	0.44	0.43	0.07
$100 < d < 220$	younger than 50 Ma	0.0	0.0	0.57	0.43
$220 < d < 400$		0.70	0.08	0.12	0.10
$400 < d < 670$		0.19	0.28	0.31	0.22
$670 < d < 1230$		0.23	0.43	0.27	0.07
$24 < d < 100$	All oceans	0.0	0.0	0.21	0.79
$100 < d < 220$	50 Ma<age<100 Ma	0.0	0.0	0.80	0.20
$220 < d < 400$		0.25	0.23	0.23	0.29
$400 < d < 670$		0.21	0.38	0.33	0.08
$670 < d < 1230$		0.21	0.46	0.21	0.12
$24 < d < 100$	All oceans	0.0	0.0	0.29	0.71
$100 < d < 220$	older than 100 Ma	0.0	0.0	0.79	0.21
$220 < d < 400$		0.20	0.42	0.28	0.10
$400 < d < 670$		0.19	0.43	0.27	0.11
$670 < d < 1230$		0.23	0.44	0.25	0.08

Table 3
Probabilities for $dlnV_s/dlnV_p$ beneath oceans. Velocity anomalies were calculated for degrees 1 to 8 with respect to PREM. The probabilities above 220 km depth are taken from [16].